JGR Solid Earth

RESEARCH ARTICLE
10.1029/2019JB019117

Key Points:
- Imaging multidisciplinary continuous deformation data to improve dike ascent modeling
- Detailed temporal model of the 2018 intrusion at Etna volcano

Correspondence to:
M. Aloisi,
marco.aloisi@ingv.it

Citation:
Aloisi, M., Bonaccorso, A., Cannavò, F., Currenti, G., & Gambino, S. (2020). The 24 December 2018 eruptive intrusion at Etna volcano as revealed by multidisciplinary continuous deformation networks (CGPS, borehole strainmeters and tiltmeters). *Journal of Geophysical Research: Solid Earth*, *125*, e2019JB019117. https://doi.org/10.1029/2019JB019117

Received 21 NOV 2019
Accepted 11 JUL 2020
Accepted article online 15 JUL 2020

The 24 December 2018 Eruptive Intrusion at Etna Volcano as Revealed by Multidisciplinary Continuous Deformation Networks (CGPS, Borehole Strainmeters and Tiltmeters)

M. Aloisi[1], A. Bonaccorso[1], F. Cannavò[1], G. Currenti[1], and S. Gambino[1]

[1]Istituto Nazionale di Geofisica e Vulcanologia - Osservatorio Etneo, Catania, Italy

Abstract We have modeled the fast dike intrusion that started on 24 December 2018 at Mount Etna. The intrusion was accompanied by an intense seismicity swarm that also continued the following day. Since previous studies did not detail the overall chain of events in time during the magma ascent, here we propose a combined analytical and FEM modeling of all available continuous deformation data, focusing on the signals over 2 days (24–25 December) when the continuous deformation networks recorded clear variations directly related to the dike ascent. High-rate GPS enabled obtaining an early and reliable source model. Borehole instruments (strainmeters and tiltmeters) highlighted clear variations, starting about 1 hr before those recorded by GPS, and moreover, made it possible to improve the dike ascent modeling. In particular, our continuous deformation data clearly revealed not one but two dikes and showed how they evolved in time. We inferred one dike that began propagating in the first kilometer above sea level, continued to rise with a maximum opening of 1.9 m and increased its horizontal dimension until reaching the ground surface. Soon after, continuous deformation networks revealed a new elongated intrusion in the southern flank, matching the south shifted position of the seismic swarm. This second dike, with a thicker opening of 4.9 m, started from a depth of about −3 km (below sea level) but did not reach the ground surface. This proposed multiparametric modeling of continuous deformation data has therefore enabled disentangling the complexity of the real volcanic processes.

1. Introduction

Mount Etna is situated on the eastern coast of Sicily (Figure 1, inset) and is affected by the collision between the African and European plates (e.g., Gvirtzman & Nur, 1999; Hirn et al., 1997). The volcano is characterized by a very complex geodynamic framework. In particular, a regional N-S compressive regime under the volcanic pile (e.g., Cocina et al., 1997), controlled by the plate collision, coexists with a WNW-ESE extensional regime, associated with the dynamics of a normal fault system located at the foot of the eastern flank, the Malta Escarpment (e.g., Hirn et al., 1997). In this framework, another local stress must be taken into consideration, namely a W-E stress due to magmatic intrusions that ascend along the volcanic pile (e.g., Cocina et al., 1998). The volcano conduit is an open system, constantly filled with magma, and showing a continuous degassing activity. Mount Etna is characterized by two main types of eruptions: (1) summit eruptions that involve the overflow of magma or explosive activity from the summit craters; (2) flank eruptions taking place along the volcano flanks as dike-forming intrusions (e.g., Aloisi, Mattia, Ferlito, et al., 2011; Bonaccorso, 2001; Bonforte et al., 2008). This last typology of eruption analyzed in this manuscript is potentially the most dangerous and represents the main hazard for the densely populated area around this volcano.

Since the 1980s, ground deformation measurements have always provided a valuable contribution to following and studying the eruptive processes, contributing to the modeling of the sources involved (e.g., Aloisi, Mattia, Ferlito, et al., 2011; Bonforte et al., 2008; Palano et al., 2017, and references therein). In the first decade of this millennium, three different intrusion processes occurred, generating the 2001, 2002–2003, and 2008–2009 main flank eruptions. The related mechanisms of the feeding dikes were studied and inferred by the deformation data (e.g., Aloisi et al., 2006, 2009; Bonaccorso et al., 2002; Bonforte et al., 2009;

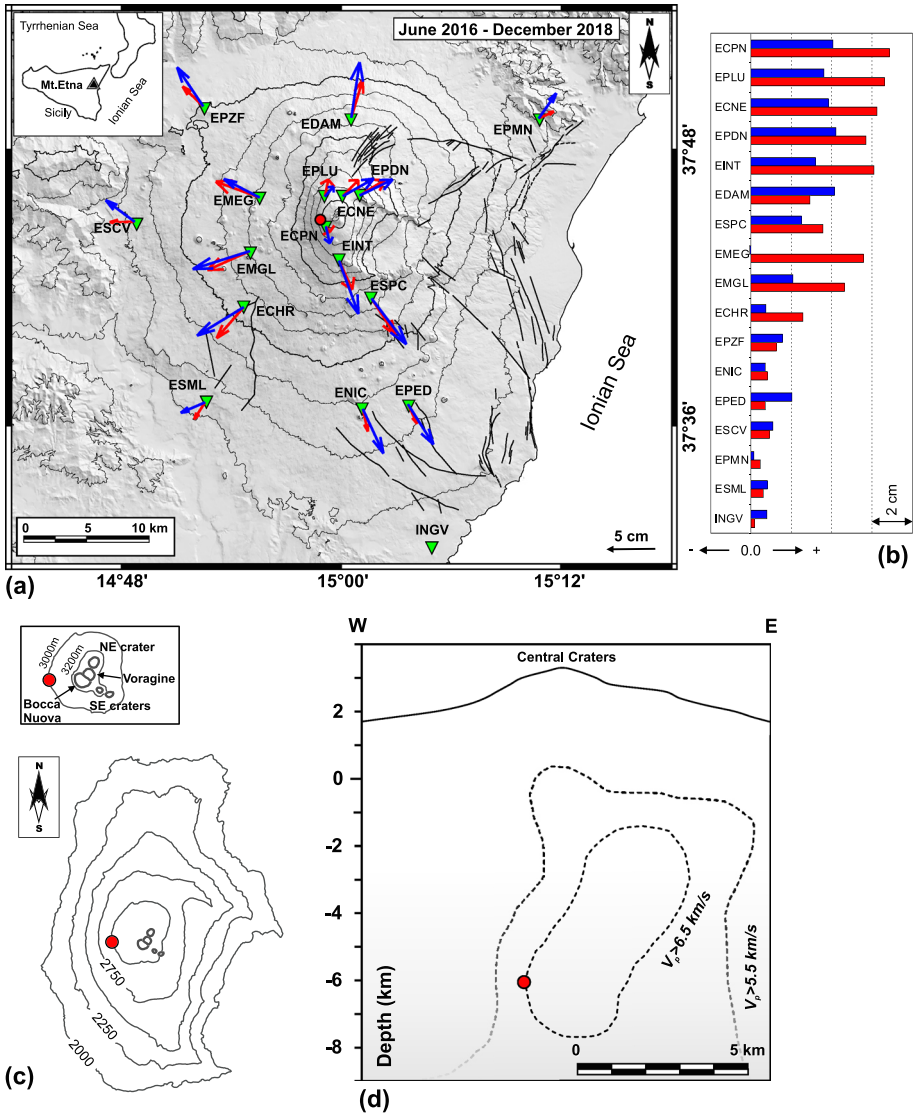

Figure 1. (a) Recorded (blue) and modeled (red) deformation pattern at Mount Etna during the recharge phase before the December 2018 eruption (June 2016 to December 2018). The histogram (b) reports the recorded (blue bars) and modeled (red bars) vertical dislocations. The vertical variations are plotted according to the CGPS station elevations. Horizontal and vertical projections (c, d) of the modeled inflation source are reported.

Carbone et al., 2014; Currenti et al., 2011; Gonzalez & Palano, 2014). The permanent deformation monitoring systems have greatly improved over the last decade. The spatial density of the permanent GPS network has increased, the resolution of borehole tiltmeters with deeper installations has improved, and, more recently, a network of borehole dilatometers has been installed. This configuration, perhaps the most advanced continuous monitoring of deformation on a volcano, has allowed us to constrain and model the fast intrusive process of 24 December 2018 that characterized the ensuing eruption, providing a possible picture of how the phenomenon occurred. The eruption was particularly intriguing as on the morning of 24 December, a rapid intrusion was detected about 3 hr before the start of the eruption, accompanied by intense seismicity which then also continued the following day (Alparone et al., 2020; Cannavò et al., 2019; De Novellis et al., 2019). This situation raised fears about a propagation of the eruptive fissure in the southern slope with possible serious consequences of feeding a lava flow even at medium to low altitudes, therefore potentially hazardous for the villages and infrastructures locat ed there. In fact, the southern sector of the volcano is characterized by a high number of eruptive vents that

have opened at low altitudes, producing numerous volumetrically important and long-lasting eruptions in recent millennia until now (Branca et al., 2011) which, if repeated, would cause enormous damage to the densely populated territory. Furthermore, from midday on 24 December, under the driving action of the intrusion, a fast acceleration of the eastern flank sliding was activated, likely promoting the destructive M_L 4.8 earthquake on 26 December in this middle flank (Civico et al., 2019). However, all these rapid and marked events were accompanied by an effusive activity with short duration (about 2 days) and a modest amount of emitted lava (about 2–3 Mm^3). This complex picture obviously raises the need for a precise and correct interpretation of the phenomena and mechanisms involved.

Currently, the only paper taking the continuous deformation at high temporal resolution into account (i.e., Cannavò et al., 2019) considers solely GPS data and thus starts the dike modeling from the first signs of deformation in the GPS time series. Here, we will show that other instruments indicated the activation of the intrusive process well before it began to be revealed by the GPS, differently from other past intrusions, like the 2001 and 2002 eruptions, for which tilt and GPS were recorded at the same time (Aloisi et al., 2003; Bonaccorso et al., 2002). Moreover, our results improve the previous interpretative models that were not based on continuous deformation measurements, but essentially considered a cumulative deformation obtained from satellite InSAR data acquired at weekly intervals (Bonforte et al., 2019; De Novellis et al., 2019; Laiolo et al., 2019). For this specific eruptive activity, the InSAR time window is too wide with respect to the fast occurrence of the intrusion and, besides the intrusive process, also encompasses movements of tectonic structures and a marked sliding of the eastern flank of the volcano.

Bonforte et al. (2019) inverted the pairs of ascending and descending interferograms acquired from 22 to 28 December. The inverted ground deformation pattern shows many features related both to the magma intrusion and to the M_L 4.8 earthquake on 26 December. Moreover, additional features related to the reactivation of other volcano-tectonic structures are visible. Therefore, these unmodeled sources can affect the final solution. The resulting model indicates that a large dike (roughly 6 km long and 4 km wide, opening 1.3 m) intruded, stopping at about sea level. The authors retain that this very big intrusion stressed the volcanic edifice and promoted the intrusion of a shallower dike (about 2 km long and 1.5 km wide, opening 0.9 m), also activating several faults. They also consider a deflating source located under the deeper dike, characterized by a volume change of about -30×10^6 m^3. Their model is unable to explain the near field, that is, the marked deformation recorded on the upper central part of the volcano. On the other hand, it explains the far field very well, that is, the deformation recorded in the middle and low flanks. Nevertheless, the use of a weekly sampling interval does not allow distinguishing the temporal occurrence of the two proposed intrusions. Our thorough analysis allows analyzing the temporal evolution of the overall intrusive process in detail.

De Novellis et al. (2019) also inverted the interferograms acquired from 22 to 28 December, as well as analyzing the seismological data. With the aim of modeling both the magma intrusion and the principal volcano-tectonic structures reactivated during the intrusive process, the authors considered more active sources with respect to the Bonforte et al. (2019) approach. Their result suggests the existence of two volcanic sources: (1) a shallow dike of roughly 3 km long, 4.5 km wide, and a maximum opening of 1.2 m; (2) a second dike source, deeper than the first one, of about 4 km long, 8.5 km wide, and a maximum opening of 1 m. With the exception of the summit variations, the model explains far and near fields well. Nevertheless, as in Bonforte et al. (2019), this approach uses a temporal resolution that fails to make a sound hypothesis on the temporal evolution of the intrusive process.

Laiolo et al. (2019) combined space and ground-based geophysical data (thermal, seismic, and infrasonic changes). The authors analyzed a long interval before the eruption onset. Regarding the intrusive process, they focused on the intervals from 29 November to 23 December 2018 and from 24 to 26 December 2018. They proposed a 2.0 km long dike whose propagation lasted for almost 3 hr. Our data clearly indicate that the intrusive process lasted longer and was more complex. Moreover, the authors hypothesized a propagation of a magma-dike injection from the central conduit toward the western rim of the Valle del Bove. This result suggests the drainage of the shallow portion of the conduit.

The goal of our study was to exploit the high-frequency ground deformation data recorded by different types of permanent networks (continuous GPS, borehole tilt, and strain). The objective was to robustly model the source that propagated during the ~2 hr and 40 min of intrusion before the eruption start

and to infer in detail the shape and mechanism of the ascending dike from the morning of 24 December until 25 December.

In particular, we will show the precise temporal evolution of the 24–25 December intrusive process that was characterized by at least two intrusions. The first reached the ground surface and fed a short-lived lateral eruption. The second dike intruded in the high southern eastern flank but did not reach the ground surface. Therefore, the permanent deformation monitoring systems clearly revealed the starting and stopping of this "hidden" dike, providing a robust early warning and, potentially, averting possible serious consequences for the villages and infrastructures on the southern slope, if this intrusion had reached the ground surface.

2. Recent Eruptive Activity and the 2018 Eruption

After the effusive flank eruption of May 2008 to July 2009, there was an extraordinary period of explosive activity at Etna volcano, with 45 lava fountains emitted from the New South East crater (NSEC) during 2011–2014 (for a review, see Calvari et al., 2018). On the basis of the erupted volumes, Bonaccorso and Calvari (2013) highlighted that the NSEC lava fountains efficiently drained the shallow storage system located at about sea level, balancing the ratio between the incoming and outgoing magma. In the following years, two sequences of four and three lava fountains occurred in December 2015 and May 2016, respectively, from the main central crater Voragine (VOR) (e.g., Aloisi et al., 2017, 2018; Bonaccorso & Calvari, 2017). Since 2015, the deformation pattern has shown a recharging phase characterized by an inflation of the volcano edifice (Aloisi et al., 2018), partially interrupted by a brief deflation associated with two explosive sequences from VOR. The displacement pattern cumulated during June 2016 to December 2018 is represented in Figure 1, and clearly show an overall inflation of the volcano edifice, testifying to its recharge phase before the December eruption. Using the same modeling approach described in Aloisi et al. (2018), we imaged the GPS baseline variations during this time interval that show a near constant crustal deformation trend. The deformation pattern is almost radially symmetric. Therefore, the pressure source has been modeled by a finite spherical magma body by using the analytical solution of McTigue (1987). The centroid of the pressurizing source is identified by five parameters: the three spatial coordinates of pressurizing source, the radius "r" and the overpressure "P" acting on the source wall, from which we derive the volume variation ΔV (Tiampo et al., 2000). The result is reported in Table 1. In particular, the pressurizing source, preparing the December 2018 eruption, is located at a depth of about 6.0 km (b.s.l.; below sea level) beneath the high western flank, which coincides with the mean depth where the modeled inflation sources are historically located (e.g., Aloisi et al., 2018) along the plumbing system (Figure 1).

From February to April 2017, the eruptive activity of Mount Etna consisted of five distinct small eruptions, lasting from 2 days to 2 weeks, characterized by Strombolian activity and weak lava flows outpouring from the crater area. The explosive activity was much less powerful than the previous lava fountains, and the summit lava flows were of small volumes. The borehole strain-meter data detected cyclic ultrasmall volumetric strain changes (~10^{-8}–10^{-9}), preceding and accompanying this moderate explosive-effusive eruptive activity (Currenti & Bonaccorso, 2019).

On 24 December 2018, after 2 months of Strombolian activity, in the early morning, the volcano was suddenly crossed by a rapidly ascending dike. The intrusion reached the surface at 11:10, generating an eruptive fissure at the base of the NSEC and characterized by explosive activity and lava flows emission (Calvari et al., 2020). In the next hours, the fissure propagated about 1.5 km, toward SE, feeding small lava flows inside the natural depression of the Valle del Bove, in the upper eastern flank (internal reports at www.ct.ingv.it). During the early morning of 24 December, the dike ascent was accompanied by a seismic swarm initially located beneath the central volcano (Alparone et al., 2020). It continued on the following days when also local faults in the SW and E flanks were activated. The most powerful M_L 4.8 earthquake occurred on 26 December at 02:19 UT in the middle SE flank along the Fiandaca fault (Alparone et al., 2020; De Novellis et al., 2019).

The eruption ended after just 2 days on the evening of 26 December, emitting 1.4 ± 0.5 Mm^3 as summit outflows and $0{,}85 \pm 0{,}3$ Mm^3 of lateral flows, as calculated from satellite spectroradiometers of MODIS and Sentinel-2 (Laiolo et al., 2019).

Despite the short duration, the December 2018 eruption triggered a very intense seismic crisis on both the SW and E volcano-tectonic structures (Alparone et al., 2020). Moreover, it promoted a strong acceleration

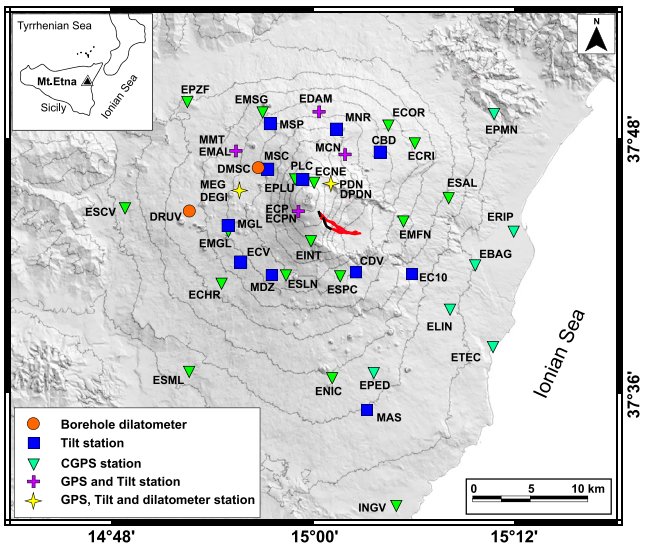

Figure 2. Map of Mount Etna showing the locations of CGPS, borehole dilatometer, and tilt stations.

of the eastern flank movements toward the SE directions. These peculiarities clearly indicate that the intrusive process was more powerful than it appeared at the ground surface.

3. Networks

3.1. GPS

The current GPS network on the volcanic edifice consists of 39 permanent stations, equipped with receivers (mostly GMX902, GRX1200, SR530 models) and antennas (mostly LEIAT504, LEIAX1202, LEIAR10 models) manufactured by Leica Geosystems (Figure 2). Along with the standard daily processing, more than half of these stations are processed in real time. In particular, the high-rate (1 Hz) raw data streams from 21 dual-frequency GPS receivers are processed on the fly by using the epoch-by-epoch algorithm of Geodetics® RTD software package (Bock et al., 2001; Nikolaidis et al., 2001). This software allows obtaining a solution every second. The chosen reference receiver is the ENIC station (Figure 2), located less than 25 km from the other stations of the network.

In this analysis, the time series of solutions were split into 10 min long windows after ascertaining this is the minimum interval to obtain a satisfactory signal-to-noise ratio. Moreover, the outliers were eliminated by using an interquartile range (IQR) filter and the multipath noise was reduced using the technique described in Cannavò et al. (2015) and Nikolaidis et al. (2001). To further increase the positioning precisions, an off-line reprocessing of GPS data was performed using the IGS (International GNSS Service) precise ephemeris.

3.2. Borehole Tiltmeters

At present, the Mount Etna permanent tilt network (Figure 2) consists of 17 borehole instruments and a long-base device installed along two 80 m long tunnels at the Pizzi Deneri Observatory (Bonaccorso et al., 2004; Gambino et al., 2014; Gambino & Cammarata, 2017). Over the last 10 years, the network has been expanded and sensors have been installed at greater depth: currently six stations are 10 m deep and eight are 27–30 m of which three are summit stations (Gambino et al., 2019). Deeper stations use biaxial self-leveling instruments (Lily and Pinnacle tiltmeters) with high-precision (10^{-8}–10^{-9} microradians), electrolytic bubble sensors for measuring the angular movement and a magnetic compass. These sensors, thanks to the installation at great depth, hence to the low noise level, also detect the tides signals (Ferro et al., 2011). Tilt stations are mostly programmed for 1 data/min, including acquisition of tilt components, ground and air temperatures and instrumental control parameters.

3.3. Borehole Dilatometers

A network of four borehole dilatometers was set up on Etna with the installations made in two successive periods during 2010–2011 and 2014 (Bonaccorso et al., 2016). The instrumentation used is the Sacks-Everson type, which detect the volumetric strain changes with a sensitivity up to 10^{-11}. The borehole dilatometers were installed in boreholes reaching depths of ~170 m (DRUV and DEGI) and ~110 m (DMSC and DPDN), respectively (Figure 2). After the first installations (DRUV and DEGI), the final response of the instruments was tested with different *in situ* calibration techniques. A first approach used the comparison between the expected and recorded strain amplitudes from the tidal strain on Earth (Bonaccorso, Currenti, et al., 2013). A second approach used the comparison between the recorded and expected strain signals from strong distant earthquakes (teleseismic $M \geq 8$) (Bonaccorso et al., 2016). Moreover, Currenti et al. (2017) also devised a new approach based on the direct comparison of the strain recorded by the borehole dilatometer with the seismic strain of teleseismic waves recorded from a nearby broadband seismic array around the dilatometer site. This third method was applied to DRUV, the most sensitive station. The dilatometers installed in the second phase (DMSC and DPDN) showed a lower sensitivity, probably due to a shallower installation depth and to the less massive quality of the rock around the bottom of the hole. To calibrate the dilatometers at DMSC and DPDN, Bonaccorso et al. (2016) calculated the signal energy ratios with respect to DRUV. They applied the discrete Fourier transform to the signals and computed the

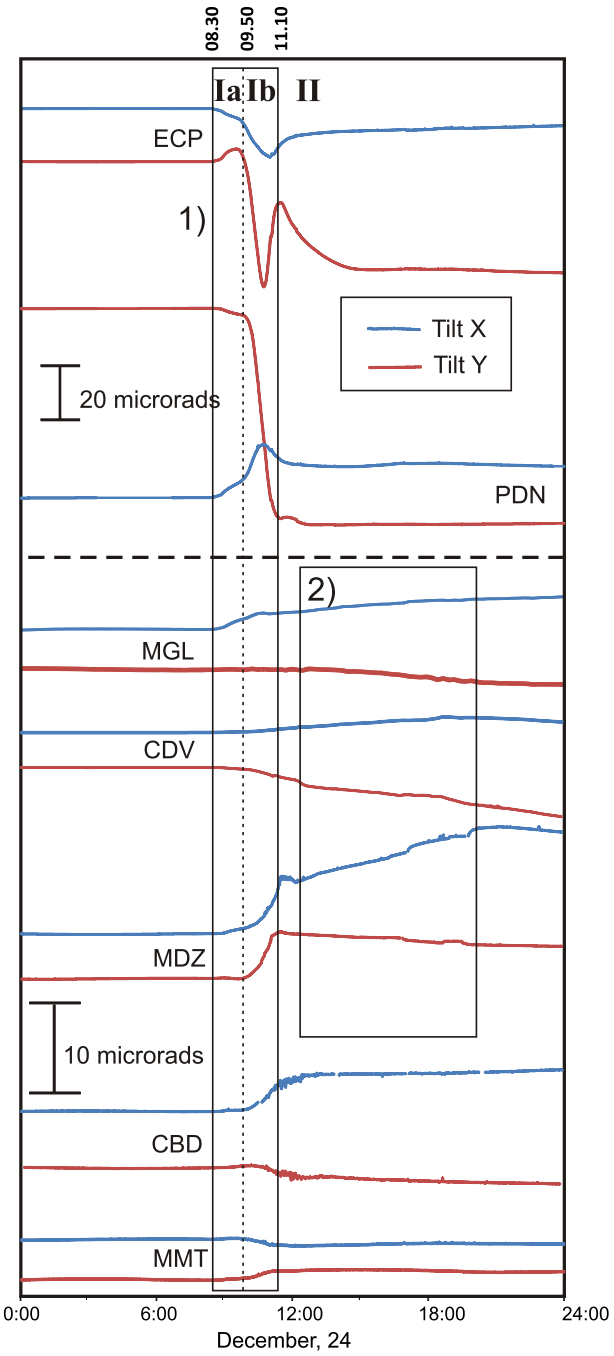

Figure 3. Tilt components recorded on 24 December 2018 at selected stations. (1) 8:20 and 11:10 UT interval where ECP and PDN recorded the strongest variations; (2) period after the 12:00 UT when significant tilt changes were recorded at the southern stations.

power spectral density to define the amplitude ratios of DMSC and DPDN signals. For a less sensitive station, similar results can be obtained by using the simple, but very effective, approach of the direct comparison with the strain signals recorded during the traveling teleseismic waves at DRUV, considered as the reference station.

4. Deformation Data

On the morning of 24 December 2018, starting from ~8:30, the borehole instruments, both strainmeter and tiltmeters, showed a significant variation in the measured signals (Figures 3 and 4), thus preceding the onset of the eruptive activity by about 2 hr and 40 min. Thanks to their precision, these variations were visible 1 hr 30 min before those recorded at GPS stations. All the signals have a first phase of marked variation up to about 11:10, when the eruptive activity became apparent from the craters and through the opening of the eruptive fissure. The strain variations continued in a second phase, even if with an attenuated pattern, until 16:30. During this last phase, further seismicity was recorded and the shallow eruptive fissure fed the overflows inside the Valle del Bove (Alparone et al., 2020; Cannavò et al., 2019).

The recorded signal changes are of considerable amplitude. Compared to the changes recorded in DRUV and DEGI during the multiple 2011–2013 lava fountains, they are even 10–15 times larger. Furthermore, DRUV and DEGI showed a continuous positive variation of strain signals (compression of the medium surrounding the instrument), which is the opposite sign to that recorded during all the 2011–2016 lava fountains. This aspect indicates that from the beginning of this phenomenon a different, more powerful source to the one feeding the previous lava fountains (i.e., the emptying of a shallow reservoir) was acting (i.e., the tensile action of the dike).

Between 8:20 and 11:10, ECP and PDN summit tilt stations recorded strong variations that reached several tens of μrads (Figure 3, box 1). Significant changes (10–20 μrads) were also recorded at PLC, MCN, and MEG, while minor variations affected other stations (Figure 3).

It is worth noting that from 12:00, significant tilt changes (about 10–15 μrads) were recorded on (Figure 3, box 2) CDV and MDZ southern stations and also evident on MGL and ECV. These slower tilt variations lasted for several hours. During this second time interval, tilt summit stations (e.g., ECP and PDN) did not record such significant variations as during the first time period.

Regarding the ground deformation field, it is challenging to pick the exact timing of significant intrusion-related ground displacement in the GPS time series. Analyzing the crossing point of the displacement time series measured at ECPN, with its moving standard deviation band (at 2σ) (Figure 5), it is possible to identify an initial weak change in the series trend between 09:30 and 9:50 and a major deviation at about 10:10, when the values went considerably beyond their standard deviation band.

After 10:30, the GPS time series showed exponential displacements, reaching the climax at about 11:10. Between 15:30 and 16:30, the GPS stations located on the south and southeast flank of the volcano edifice (e.g., EINT and ESLN, Figure 5) underwent a further displacement. This new deformation would suggest a further tensile opening along the southern part of the alignment of the previous dike.

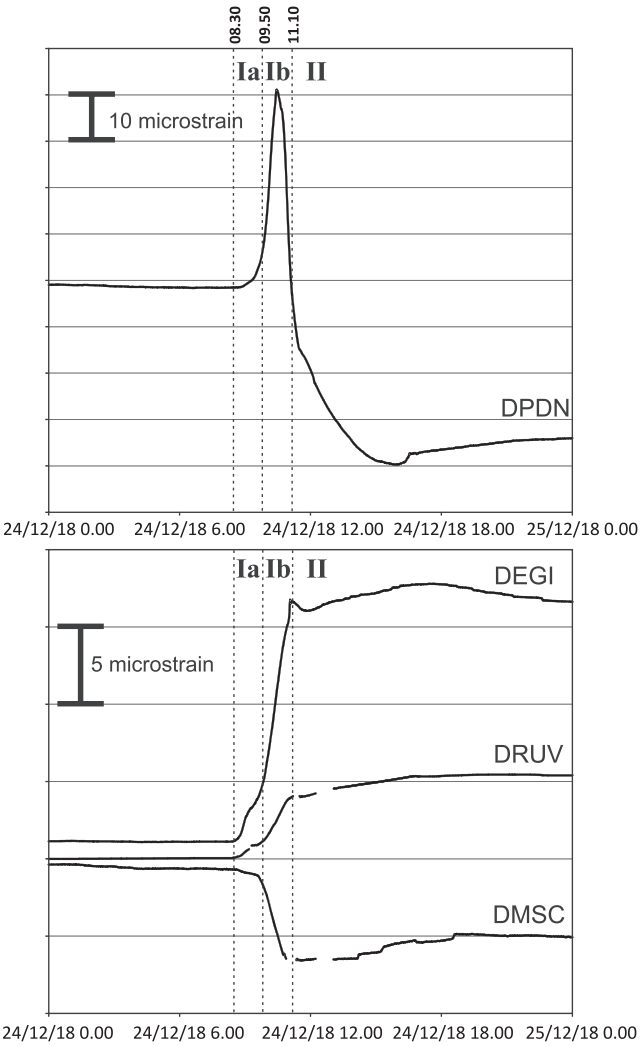

Figure 4. Strain signals recorded at the borehole dilatometer stations.

5. Modeling

5.1. First Result

At the beginning of the eruption, the intrusion was evident from the real-time GPS data that are the only deformation signals actually implemented in the real-time modeling system. Indeed, the cumulated displacements indicated a typical pattern of dike opening even before the effusive fracture opened at the surface and was visible from the monitoring thermal cameras (Cannavò et al., 2019).

In order to quickly assist the Italian Civil Protection Authorities in understanding the ongoing event, we provided a first estimation of the dike model during the initial phase of the eruption. By using exclusively the GPS solutions processed in real time at high frequency and the algorithm to invert those data (Cannavò, 2019), we estimated a subvertical dike located right below the eruptive fractures (with an azimuth of 164°N) at about sea level, with a horizontal length of 2 km, a vertical width of 1 km and an opening of 3 m (Figure 6). The model of this first dike was then refined including more reliable displacement estimations, though it never diverged much from the initial estimation.

5.2. Data Integration and Improved Modeling

Using an analytical approach, we tried to refine the first result obtained (section 5.1) by modeling three different typologies of ground deformation data together, namely GPS, tilt, and strain, recorded during the December 2018 volcanic activity. As above mentioned, each kind of data is characterized by a different level of accuracy, which means that each different type of station can detect different parts of the overall process of intrusion. In fact, strain and tilt variations started about 1 hr 30 min before GPS variations (Figure 7). We found that the first modeling solution obtained exclusively using the GPS data (section 5.1) was unable to clearly explain the tilt and strain variations recorded in the same time interval. This is probably because these two kinds of sensors also recorded some contribution of the intrusive process that was not contemporaneously detectable by the GPS network. Maintaining the simplicity of the analytical approach, with the aim of obtaining an effective mean representation of the intrusive process, we separated the intrusion into three time intervals:

(Ia) the first phase of intrusion from 24 December at 08:30 UT, when tilt and strain variations began, until 24 December at 09:50 UT, when GPS stations also started to show the first significant signals, over the background noise;
(Ib) the phase of intrusion between 24 December at 09:50 UT (all stations recorded significant variations) and the opening of the eruptive fissures, 24 December at 11:10 UT;
(II) the final phase of the intrusive phenomenon, from 24 December at 11:10 UT to 25 December at 16:00 UT, when a new intrusion was recorded in the southern flank of the volcano (Figure 8).

With the aim of modeling the recorded deformation patterns, we performed three independent analytical inversions using the rectangular dislocation in an elastic, isotropic, and homogeneous half-space described by Okada (1985). The model comprised the following eight parameters: spatial coordinates of the top center (x, y, z), dimensions of the dike (horizontal length and vertical width), spatial orientation (azimuth referred to the north direction and dip referred to the free surface) and, finally, opening of the dike surfaces. For each phase, we estimated these parameters performing an analytical inversion by means of the Pattern Search technique (Lewis & Torczon, 1999) used jointly with the local Genetic Algorithm Search (Goldberg, 1989). In order to refine the solution, we also applied a nonlinear least squares optimization (Cannavò, 2019). The simultaneous inversion of different data sets was performed by minimizing the reduced chi-square statistic normalized for the number of stations for each kind of data. This was necessary to allow data from

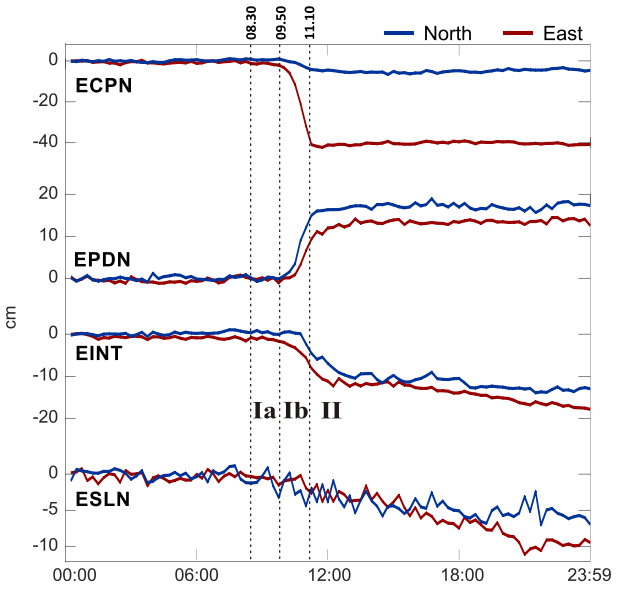

Figure 5. Time series of horizontal components of four GPS summit stations on 24 December 2018, sampled every 10 min. It is possible to see that the beginning of the instrumentally appreciable deformation starts from around 10 UT.

different network sizes to give the same contribution to the error. Moreover, the algorithm we adopted to invert the data (Cannavò, 2019) does not provide the PDFs of the model parameters. Therefore, the Jackknife resampling method was adopted to estimate the uncertainty of each parameter (Efron, 1982). We did not include the effects of the topography, deferring this detail to the following FEM approach (see the next section). The medium was assumed to be characterized by typical elastic modules: Young modulus of 75 GPa and Poisson ratio of 0.25 (Aloisi, Mattia, Monaco, et al., 2011).

In the inversion process, we excluded the tilt station MCN positioned on the active lineaments of the NE rift and the two stations, DEGI (strainmeter) and MEG (tilt station), which are colocated at the same site showing a strong local tilt/strain response that cannot be modeled using a simple elastic half-space rheology. Moreover, we excluded the ECV tilt station because it is located between two active local lineaments as evidenced by Catalano et al. (2013). This discontinuity belongs to the fault system located south of ECV and visible in the InSAR image (Bonforte et al., 2019), and it could have distorted the tilt signal.

The summit area, the zone delimited by the PLC, PDN and ECP sites (Figure 2), is characterized by several factors that can complicate the deformation response, including the extreme lack of coherence of the medium, the presence of discontinuities on which the craters are located, and the markedly steep topography. After numerous trials, we verified that for a dike propagating in the last shallow portion of the volcano edifice (i.e., the last hundreds of meters under the craters) the strain and tilt in the summit area are sensitive in response both to the different horizontal extension of the dike and to its possible variation in azimuth. A slight change of the dike dimension and/or a few degrees rotation of its direction can significantly change the response of the tilt and strain in the summit area in amplitude and even in sign. However, the biggest distorting effects, and more complicated pattern, are expected for the strain at DPDN (more details are given in section 5.4). For these reasons, in the inversion we did not consider the DPDN strainmeter summit station.

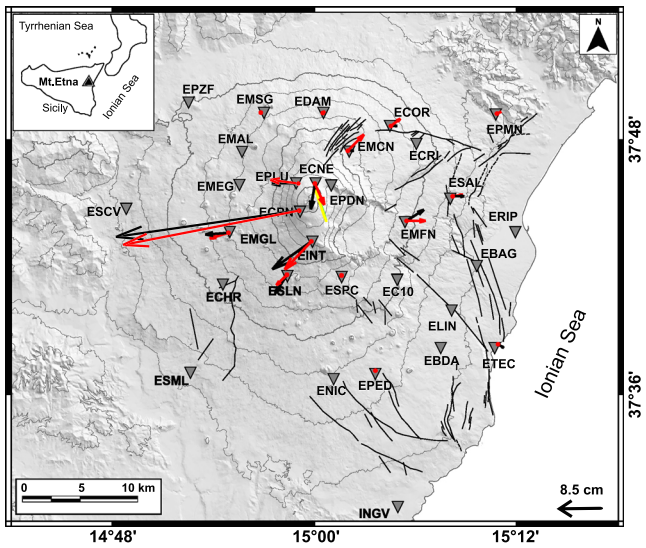

Figure 6. Comparison between observed (black arrows) and modeled (red arrows) horizontal geodetic displacements measured and modeled in the interval 8:30–12:00 UT (exclusively the GPS solutions inverted). The yellow segment indicates the location of the early-modeled source.

The phase (Ia) represents the first part of the intrusive process clearly detected by the most sensitive borehole networks (Figure 7). It took place at about sea level (Table 1 and Figure 9) with a volumetric expansion of about 1.2×10^6 m^3. The tensile dislocation is located roughly below the zone where eruptive fissures would open within a few hours and, characterized by a dip angle of 90°, suggesting a near vertical rising of the dike-forming intrusion. The model explains well the data recorded at the summit tilt stations and partially the signals observed at the remaining tilt stations, located at a lower altitude.

Regarding the second phase (Ib), this represents the continuation of the intrusive process (Ia) from the sea level toward the ground eruptive fissures. We constrained the vertical dimension (width) of the tabular structure (Ib) from the top of the (Ia) model to the ground surface. We limited the maximum value for the horizontal dimension (length) of the dike-forming intrusion (Ib) to the length of the eruptive fissures. The second phase is compatible with a near vertical dike-forming intrusion, bigger than the planar dimensions of the (Ia) model (Table 1 and Figure 9). It is characterized by a volumetric expansion of about 4.9×10^6 m^3. As regards vertical variations recorded at the GPS network, we observed very small values (few centimeters) with respect to the horizontal dislocations. This testifies to a dominant tensile mechanism without the need to consider the contribution of a further pressurization or depressurization source.

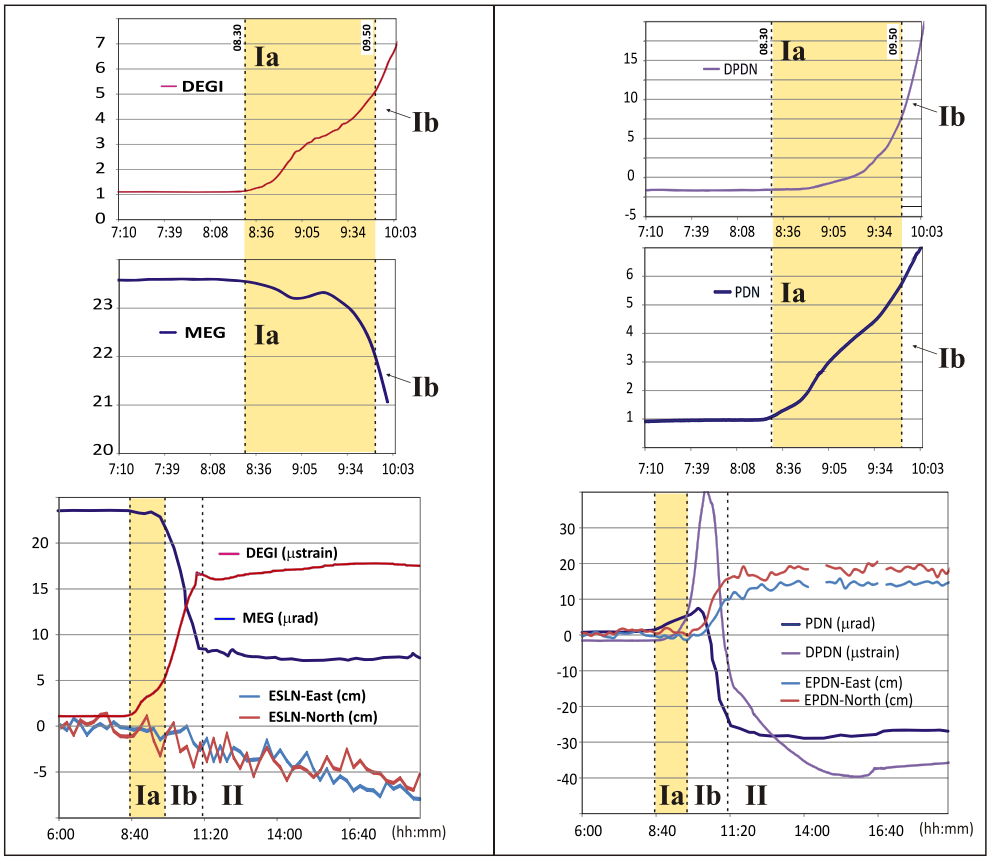

Figure 7. Comparison of signals from colocated stations of CGPS, borehole strain, and tilt. On the left, the strain (DEGI) and tilt (MEG) recorded at the same site, Monte Egitto, on the middle W flank, and the CGPS on the SW flank (ESLN) are reported. On the right, the CGPS (EPDN), strain (DPDN), and tilt (PDN) signals recorded at the same summit site of Pizzi Deneri (2,800 m above sea level).

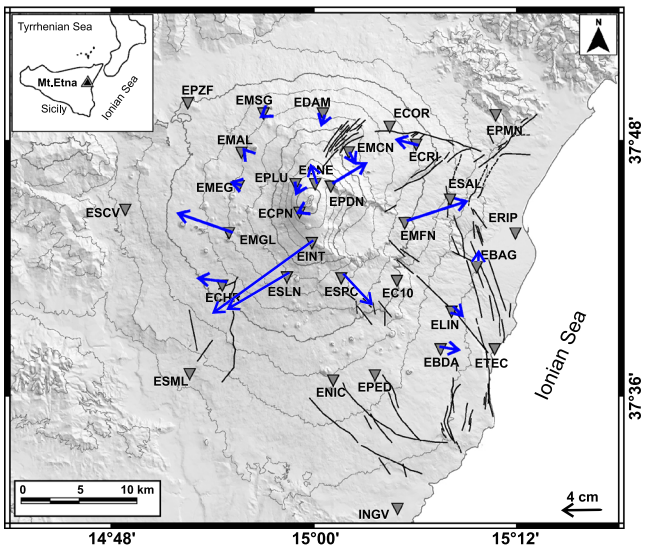

Figure 8. Horizontal geodetic displacement field measured in the time interval (II) (from 24 December at 11:10 UT to 25 December at 16:00 UT).

To sum up, the results obtained for the phases (Ia) and (Ib) indicate that the magmatic intrusion ascended near vertically from the sea level toward the ground surface where eruptive fissures opened, gradually increasing its horizontal dimension ("Length" parameter in Table 1).

After the opening of the eruptive fissure, the GPS network observed significant variations in the southern sector, cumulating about 0.1 m in about a day (phase (II)). The recorded deformation pattern is characterized by divergent dislocations of the GPS stations on the midsouthern flank (Figure 8), which is compatible with a tensile action of a new intrusion below this area. To model this phase, we did not use the GPS stations located on the lower eastern flank of the volcano as it is affected by an ESE-ward sliding dislocation, sometimes influenced by magmatic processes (e.g., Aloisi, Mattia, Monaco, et al., 2011). Moreover, the entire GPS network recorded a clear downlift probably due to the ongoing effusive activity (Figure 9h). Therefore, to model phase (II), we used contemporaneously a tabular dislocation and a depressurization source (Mogi, 1958). We constrained this depressurization area to the zone where deflation sources are historically found (Aloisi et al., 2018). This zone of the plumbing system is located roughly below the crater area, at a depth of about 4.5 km (b.s.l.). A source volume variation of about −5 Mm^3 of magma is enough to explain the downlift observed at the GPS network.

Table 1
Model Parameters and Related Uncertainties

Parameters	Recharching phase (June 2016 to December 2018) McTigue (1987)	Phase Ia (24 December 08:30–09:50 GMT) Okada (1985)	Phase Ib (24 December 09:50–11:10 GMT) Okada (1985)	Phase II (24 December 11:10 GMT to 25 December 16:00 GMT)	
				Okada (1985)	Mogi (1958)
Invert. param. / source param.	5/5	8/8	7/8	8/8	1/4
x (m)	498,375 ± 1	500,356 ± 350	501,166 ± 168	499,941 ± 1,578	499,748 (fixed)
y (m)	4,177,924 ± 1	4,177,834 ± 204	4,177,846 ± 338	4,174,530 ± 620	4,178,440 (fixed)
z (m)	−6,048 ± 2	+436 ± 630	+2,000 ± 189	+1,544 ± 450	−4,500 (fixed)
Length (m)		675 ± 514	2,700 ± 526 (max value fixed)	580 ± 359	/
Width (m)	/	977 ± 364	1,500 (fixed)	4,374 ± 1,553	/
Azimuth (°)	/	160 ± 2	159 ± 6	174 ± 23	/
Dip (°)	/	89.9 ± 0.7	89.9 ± 0.5	89.9 ± 0.0	/
Opening (m)	/	1.9 ± 0.5	1.2 ± 0.6	4.9 ± 1.2	/
ΔV (m^3)	*2.4E+7 (derived)*	*1.2E+6 (derived)*	*4.9E+6 (derived)*	*1.2E+7 (derived)*	−5.2 ± 2.8 E+6

Note. The McTigue (1987) source volume ΔV (italicized data) is calculated according to the Tiampo et al. (2000) formula, using a value of the effective shear modulus μ equal to 30 GPa. The "z" parameters are reported with respect to sea level.

The deformation pattern of this second phase is compatible with an elongated, near-vertical, dike-forming intrusion located below the high southern flank. Characterized by a volumetric expansion of about 12×10^6 m^3, it started from a depth of about −3 km (b.s.l.) and stopped, inside the volcano body, at a height of about 1.5 km (a.s.l.; above sea level), see Table 1. Therefore, this dike, characterized by a powerful opening with respect to the first dike, fortunately did not reach the free surface located 1 km above its tip.

The second phase ceased definitively during the early hours of 25 December, giving way to the acceleration of the eastern flank sliding, while the eruption ended 2 days later.

5.3. Examination of Numerical Modeling

The data analysis and modeling of the first phases clearly indicated the magma ascent from a shallow level toward the surface, initially detected only by the borehole sensors during phase (Ia) and then tracked also by the GPS data in phase (Ib). The real shape and opening of the dike during its ascending intrusion depends on the mechanical response of the surrounding rocks to the magma overpressure along its path. Because of volcano topography and medium heterogeneity, the dike is not a perfectly rectangular and regular tensile dislocation, such as modeled by using the first-order approximation of the analytical solution. Therefore, to obtain a more detailed source model, a FEM-based procedure was applied to invert the geodetic data in the phases (Ia) and (Ib). Moreover, the numerical approach allowed verifying if the discrepancy between data recorded and data modeled by the previously described analytical approach is solved using a more realistic geometry (topography and medium heterogeneity).

A distributed opening source model was explored by considering a planar surface, constrained by the analytical solution and large enough to include the magmatic intrusions (Ia) and (Ib). It extends 3000 × 3000 m and reaches the ground surface. In particular, the planar surfaces, obtained from the analytical inversions in phases (Ia) and (Ib) (Table 1), are very similar to each other within uncertainty. Therefore, we used the same vertical planar surface for both phases. The surface was subdivided into 100 patches of 300 × 300 m. The deep patches are regular rectangles, while the shallower ones follow the topographic relief. Pair elements are applied to represent the tensile dislocation (Currenti et al., 2008). The static elastic Green's functions for each patch were computed by solving a 3-D FEM elastic problem, in which a unity tensile opening is assigned sequentially to each patch and null openings to all others belonging to the source (Currenti et al., 2012). The 3-D FEM was solved using the COMSOL package by implementing specific subroutines for automatic sequence execution in preprocessing and postprocessing computation. The domain geometry takes

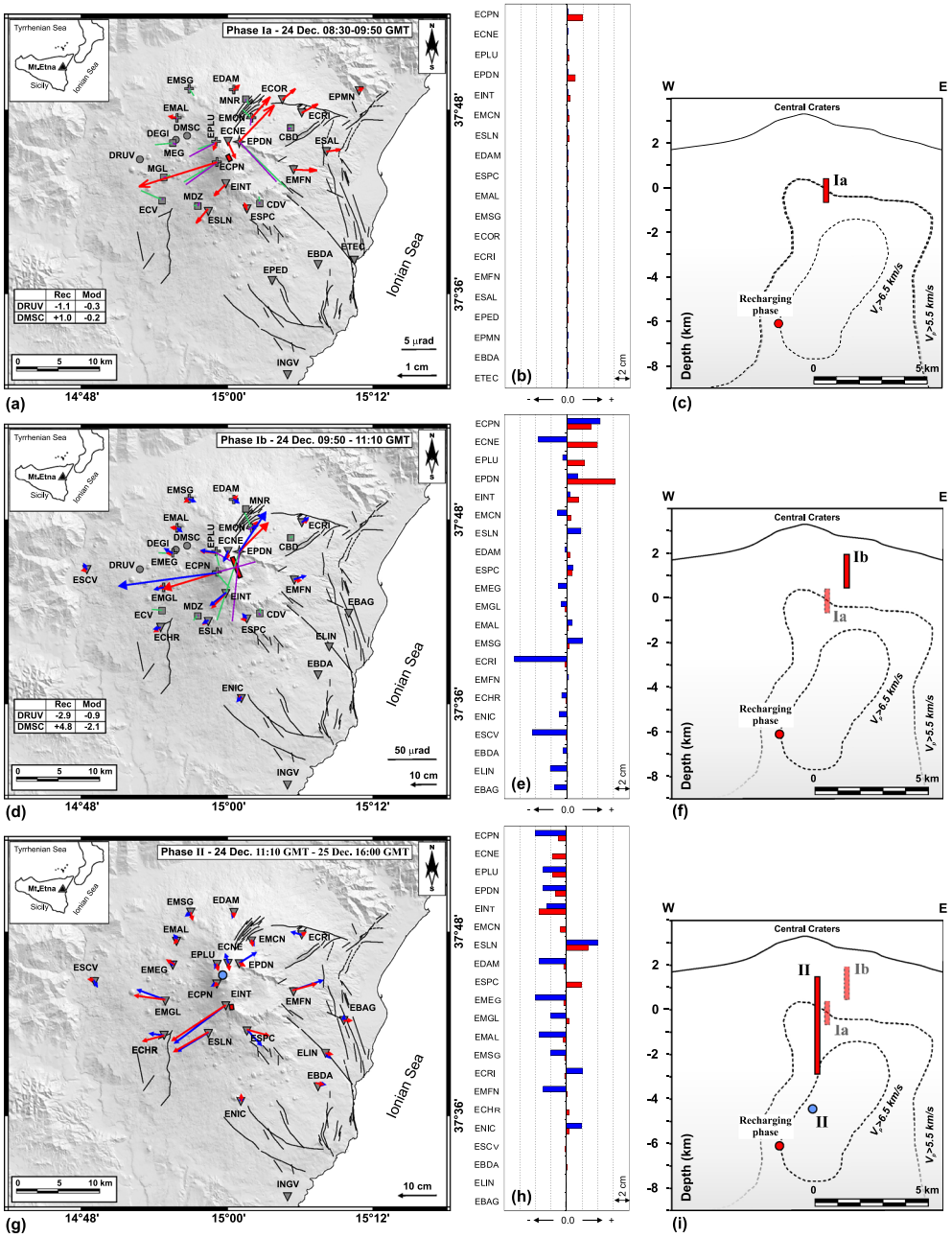

Figure 9. (a, d, g) Recorded (blue) and modeled (red) GPS displacements and modeled (purple) and observed (green) tilt vectors at Mount Etna for phases (Ia), (Ib), and (II), respectively. The histograms (b, e, h) report the recorded (blue bars) and modeled (red bars) vertical dislocations for each phase. The vertical variations are plotted according to the CGPS station elevations. Vertical projections (c, f, i) of the modeled sources are shown along a WE vertical plane passing through the central craters. For DEGI strain values see text, for DPDN strain values, see section 5.4.

into account the Etna volcano topography and elastic medium properties derived from seismic tomography (more details in Currenti et al., 2008). The 3-D computational domain extended 30 × 30 km and was meshed into 181,894 isoparametric and arbitrarily distorted tetrahedral elements. Around the source, a finer mesh (60 m) is applied, which then gradually increases going toward the external boundaries, where infinite mapped elements are used to force the displacement to vanish toward infinity. Quadratic elements were chosen to warrant a good accuracy in the computations of first spatial derivative of the displacement fields, necessary to estimate tilt and strain changes. After computing the Green's functions, a linear inversion problem was resolved to estimate the dike opening distribution from strain, tilt and GPS vector

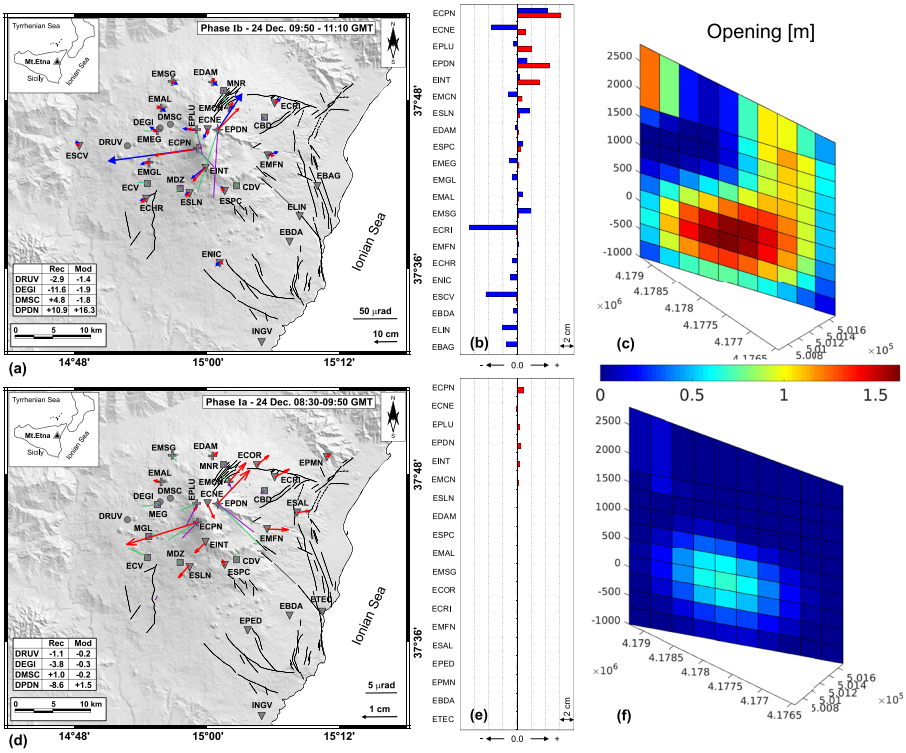

Figure 10. Modeling results using a FEM inversion of GPS displacements, tilt, and strain changes from 08:30 to 9:50 (phase (Ia); d, e) and from 09:50 to 11:10 UT (phase (Ib); a, b). Comparisons between modeled (red) and observed (blue) horizontal GPS displacements and modeled (purple) and observed (green) tilt vectors, show a general agreement in the overall pattern. Vertical displacements are reported as well (b, e). Tensile opening distributions show the magma upward migration starting from sea level (phase (Ia); f) toward the surface (phase (Ib); c), where eruptive fissures opened.

data. The system of linear equations was solved using a Quadratic Programming (QP) algorithm. To stabilize the solution, bound constraints, between 0 m and 2.5 m, were set and a smoothing functional based on the second-order spatial derivative was used (Currenti et al., 2010).

The opening distribution in phase (Ia) shows a concentration of opening at 0 m b.s.l. in the initial phase of the intrusion (Figure 10f). From the estimated opening distribution, with a maximum value of about 0.7 m, a volume change of about 1.14×10^6 m^3 is estimated, which is similar to that obtained from the analytical inversion (Table 1; 1.2×10^6 m^3). A more complex pattern is instead obtained in phase (Ib), that clearly shows the migration of magma toward the surface from the overpressurized volume identified in phase (Ia) (Figure 10c). The opening distribution reaches a maximum value of about 1.6 m, leading to a volumetric expansion of 7.0×10^6 m^3, greater than the value obtained by the analytical approach (Table 1; 4.9×10^6 m^3), but still within the estimation error for this parameter, as evidenced by Cannavò et al. (2019).

By comparing the numerical model with the analytical one, the match with observed data is improved in some stations, even if the fit worsens in others. In phase (Ia), we verified that horizontal and vertical displacement components were below 1 cm, hence below the associated uncertainty of GPS-HF solutions. In the overall pattern, significant discrepancies are observed in tilt and strain data at some stations, where local high complexity of the medium, not comprised in the FEM domain, may induce small-scale spatial variability (see next paragraph for more details).

5.4. Discrepancies in the Summit Area Records

The integrated inversion of data from various geodetic sensors (GPS, tiltmeters and strainmeters) was not straightforward for the stations in the summit area. As aforementioned, the sole inversion of GPS data (section 5.1) proved fairly robust but provided a solution that does not justify the tiltmeter and strainmeter observations. The difficulty in finding a unique solution, able to match all the data, may arise from the simple

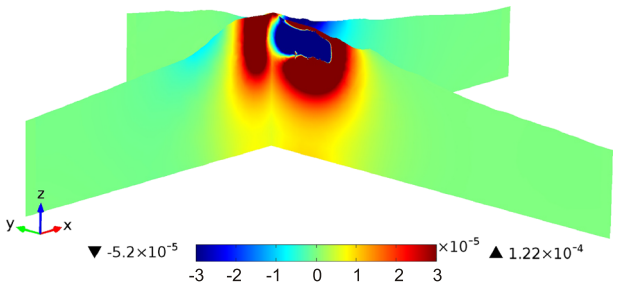

Figure 11. FEM-based computations of the volumetric strain induced by the magmatic intrusion in phase (Ib). The complex pattern of the strain field is highly sensitive to topography, medium heterogeneity, and magmatic intrusion geometry. The two vertical perpendicular sections pass across the DPDN strainmeter station. Maximum and minimum values are also reported.

model used to represent a fast magmatic intrusion at very shallow depth crossing the ground surface in a prominent relief.

As evidence of this, regarding the summit area, if we compare Figure 9d and Figure 6, it is clear that the fit at the ECPN GPS station worsened in the cumulative inversion (Figure 9d) with respect to the inversion relative to the GPS data alone (Figure 6). But, as mentioned, this step is necessary because the first solution obtained solely for the GPS data is not able to explain the ECP tiltmeter, and, generally, the other types of data. Therefore, the cumulative solution is a compromise for which the limit of the available models to explain all aspects of the intrusive process and its interaction with the surrounding, very complex medium, is clearly evident. For example, the ECP tiltmeter station (Figure 3, box 1) showed a clear inversion for the Y component. In the cumulative modeling, we excluded this data inversion, considering exclusively the step variation before and after. We verified that this peculiar tilt change can probably be explained by the uprising process of the dike, when it reaches the pellicular zone of the free surface (about a few hundred meters), producing localized strong dislocations (several meters). However, these specific processes are not easily modeled when looking at the entire uprising process.

Similar difficulties are encountered in explaining the strainmeter data. Indeed, strain and tilt components, being spatial derivative quantities, are very sensitive to small-scale heterogeneities and topography. With the aim of displaying the complexity in the modeling procedure of the solutions, here we report the numerical FEM solution computations of the computed volumetric strain in the summit area. Figure 11 shows the volumetric strain induced by the magmatic intrusion in phase (Ib), modeled as a shallow rectangular tensile dislocation. The two vertical perpendicular sections pass across the DPDN strainmeter station. It is worth noting that the geometry of the magmatic source, its orientation, and the volcano topography, induce abrupt volumetric strain variations in the summit area, from positive to negative values. While ground deformation patterns are generally smooth, strain variations for such a shallow source could be very sharp in the area near the intrusion. Due to the shallowness of the source and the position of the DPDN station, slight variations in the source geometry may engender very significant variations in estimating the strain. Moreover, local discontinuities and structures, not well known and difficult to include in a model, may also play a role in enhancing the discrepancies.

6. Discussion and Final Considerations

The continuous data of the multidisciplinary deformation networks first enabled an immediate contribution to understanding the ongoing eruptive process, which is of great support to the Civil Protection Authorities, and second, the possibility of a reliable and timely modeling able to constrain the complex intrusion mechanism.

Concerning the first issue, the high-precision borehole strain and tilt changes recognized a first variation at about 8:30 a.m. This aspect is important to support the interpretation of other data (onset of the seismic swarm). Moreover, from the onset of the intrusive process, the sign of the variation in the strain signals at the more distant stations allows distinguishing the type of source, recognizing the tensile action caused by a magmatic intrusion. The frequent updates sent to the Italian Civil Protection Authorities on the ongoing volcanic activity, as described in section 5.1, included a first estimation of the dike model using exclusively the GPS solutions, as only the real-time modeling of GPS data is actually implemented in the early warning system. Our detailed a posteriori analysis of the 24 December 2018 intrusion, clearly showed that, as the goal of a future challenge, it is important to also integrate the real-time modeling of borehole data in the early warning system together with the real-time modeling of the GPS data.

To the best of our knowledge, this work is the first attempt to jointly analyze and model GPS, tiltmeter, and strainmeter data together during a dike intrusion. Our results have highlighted that the spatial deformation pattern is fairly regular, whereas tilt and strain changes are rather uneven at some stations, preventing obtaining a good overall fit when all data are jointly inverted. The most significant discrepancies arise at stations located in the summit area and near structural lineaments (likely activated during the seismic crisis

accompanying the eruption). Accounting for topographic effects and medium heterogeneity by means of numerical models (Bonaccorso, Currenti, et al., 2013) does not help resolve the discrepancies at some stations (e.g.m MEG, ECV, DEGI, and DPDN). Therefore, other local effects, not considered in the FEM model, can produce strong variations in the spatial derivative of the displacement field (tilt and strain values).

In particular, these discrepancies may reflect minor and local readjustments of local lineaments and/or discontinuities following stress generated by magma propagation, which may be captured only by high-precision measurements. In this context, the GPS proved to be the most effective single method to provide a clear indication of a fast intrusion mechanism (tensile dike) and, above all, to constrain its shape and position in the final path crossing the volcanic edifice.

Concerning the second challenge on efficient and timely modeling, only continuous monitoring data may satisfy this request, clearly discerning every single phenomenon of a complex "chain of events." Previous studies sought to model the deformation observed by remote sensing. The overall deformation pattern as seen from satellite DInSAR data suggests the action of a bigger intrusion. By using data from Sentinel-1 acquired in the time interval 22–28 December, Bonforte et al. (2019) found a main dike vertically elongated about 4 km and stopping at near sea level, successively promoting the intrusion of a shallower dike. But these sources are unable to cause the marked deformation recorded in the summit zone of the volcano. With the same data, De Novellis et al. (2019) also suggest the presence of two near-vertical dikes, one shallower and the other deeper, without providing their temporal evolution. In fact, the DInSAR data are hindered by the large window of the measure time interval (near a week) to calculate the ground deformation. For the 2018 eruption case, this aspect caused two main limitations. First, the data were not promptly available to provide information during the onset of the eruption, when Civil Protection Authorities needed timely scientific support. Second, the interval of 22–28 December covers 4 days after the intrusion. During the days following the 24 December intrusion, in response to the tensile action, the entire portion of the east flank started to slide toward E (e.g., Aloisi et al., 2019). This is testified by the seismicity of the following days released in response to the flank movement (Alparone et al., 2020). Therefore, the DInSAR measured the superposition of different effects (intrusion, flank sliding, and volcano-tectonic structures reactivations). This weakens the DInSAR modeling for this specific case of the very fast intrusion occurring in the early morning of 24 December. On the other hand, in Cannavò et al. (2019), the authors inverted only the high-rate GPS data to reconstruct in time and space the dike intrusion from its early stage to its propagation, and constrained by means of infrasound data the interaction between the dike and the central plumbing system. The resulting dike is consistent in geometry, position, and opening with the models proposed here for the phases (Ia) and (Ib), while it differs in phase (II) where the authors suggest a southward propagation and a simultaneous deepening of the same shallow dike instead of a new intrusion pulse from depth. However, their inversion is spatially and temporally constrained by Laplacian operators, while here we have considered the phases as completely independent. Nevertheless, both inversions agree in showing that the (Ib) phase reaches a shallower elevation compared to the southern portion of the intruding dike in phase (II). The spatial separation between the two intrusions (Ia) and (Ib) and (II) is clearly highlighted by two separated clusters of earthquakes recorded during these phases (Alparone et al., 2020; their Figures 4c and 5a). Their results also showed that the earthquake cluster related to the period when the (II) intrusion took place (24 December at 11:10 UT to 25 December at 16:00 UT) is deeper than the cluster related to the first phases of the intrusion (from 24 December at 08:30 UT to 24 December at 11:10 UT). Recently, also Giampiccolo et al. (2020) observed a stress increase in the eastern flank, roughly between 0 and 3 km (b.s.l), caused by the dike intrusion. This depth range is compatible with the vertical position of our dike (II). Moreover, in accordance with our result that the dike (II) stopped below sea level, Alparone et al. (2020) found that the related cluster showed a prevailing normal faulting mechanism consistent with a powerful magma push from a deep pressure source.

In our study, we highlight that the continuous monitoring networks provided robust data allowing to understand the fast eruptive process taking place during the early stage (few hours) of dike intrusion and eruption, improving on the previous results and providing a more realistic interpretation of the "chain of events."

We inferred a first dike starting from the sea level depth (phases (Ia) and (Ib)) with an increasing of its dimension in the shallower part (Figure 12). It is interesting to note that the sea level is the depth of the small shallower reservoir that fed the tens of lava fountains from NSEC crater during 2011–2013. This shallow

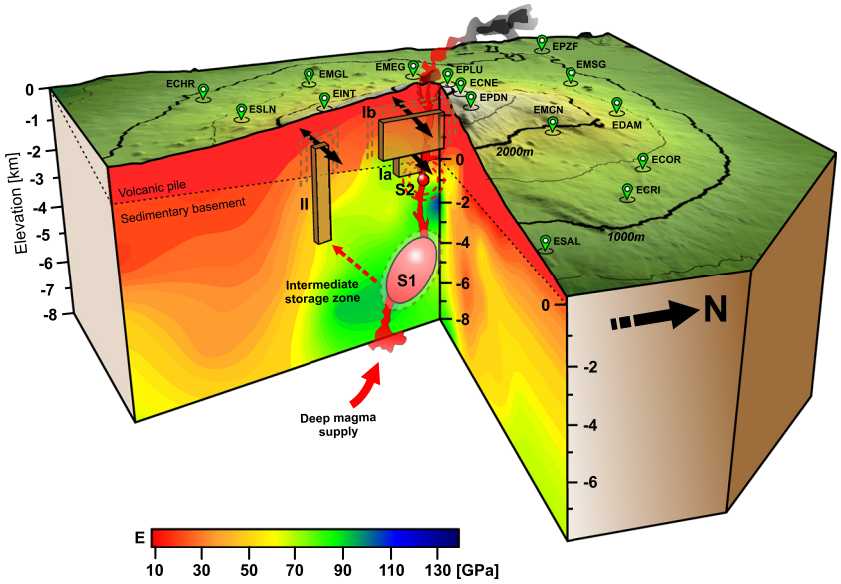

Figure 12. 3-D sketch map showing the model for processes occurring at Mount Etna before and during the December eruption. S2 is the shallow storage source that fed the tens of lava fountains during 2011–2013. S1 is the intermediate storage zone corresponding to the inflating source acting during the recharging phases, such as during the 2016–2018 period. (Ia) is the first part of the shallow dike propagating from S2 under the push of S1; (Ib) is the final part of this dike, reaching the surface and generating the lava output. (II) is the second deeper dike that stopped below the ground surface and did not cross the final portion of the volcano edifice. See text for the detailed parameters and modeling description.

source of the lava fountains was modeled by the strain changes revealed by the high-precision borehole strainmeters. The numerical computations indicated a depressurizing source located at 0 km b.s.l., which underwent a volume change of ~2 × 10^6 m^3, roughly the magma volume erupted, excluding a smaller remaining part of ~0.5 × 10^6 m^3 that is accommodated by the compressibility (Bonaccorso, Currenti, et al., 2013; Bonaccorso et al., 2014). Therefore, the first eruptive dike (Ia) departed from the source that previously generated the NSEC lava fountains and discharged the magma volume that could be stored in this shallow reservoir. The physical process involving the formation of a lava fountain follows the foam collapse model of Jaupart and Vergniolle (1988), which considers the formation and accumulation of a bubble foam layer. Bonaccorso et al. (2011) and Bonaccorso, Calvari, et al. (2013)proved that the regular magma ascent can generate a bubble-rich magma (foam) in the upper level of the shallow storage zone that can be released through cyclic paroxysmal episodes in the form of lava fountains. But this time, the 2018 eruption, although setting off from the same shallow source, was not evidently driven by an accumulation/release of a fluid rich enough in gas to generate a lava fountain. This eruption, differently to a lava fountain, must have been generated by an intrusion of previously accumulated magma, less rich in gas, able to exert a strong tensile action with the propagation of an eruptive fissure. This superficial source of modest dimensions in both cases (2011–2013 lava fountains and 2018 dike) produced a limited emptying, emitting a few millions of cubic meters of magma.

However, during 2016–2018, the main pressure was exerted on the entire volcanic edifice from the recharging of the main intermediate storage inferred at ~6 km b.s.l. (Aloisi et al., 2018). We retain that this main source stimulates the small shallow reservoir that produces the shallow dike of phases (Ia) and (Ib), but was also able to break the intermediate storage and attempted to penetrate the volcano edifice through an elongated and thicker dike from this deeper level, as evidenced by the modeled intrusion of phase (II) (Figure 12). This second attempt of intrusion was also accompanied by the depressurization of the intermediate storage zone from which the dike started to propagate toward the surface (Figure 12). Finally, it is interesting to observe how the deep dike, although very thick (i.e., ~5 m opening), caused unmarked surface effects on the entire volcanic edifice, but instead the deformation was detected only in the southern flank portion above its projection. Two factors explain this behavior: (i) the dike stopped below the

ground surface and did not cross the final portion of the volcano pile, and (ii) its relatively small horizontal dimension (about 600 m), compared to the shallow dike (Ib) (about 2,700 m). If the deeper dike had been >1.5–2 km longer, it would have caused marked deformation on the scale of the entire volcano edifice. Because of its decentralized location, this dike could have been a significant hazard if it had reached the surface. Fortunately, this did not happen probably because most of the energy was already released in the first intrusion and the resulting eruption. In fact, this hypothesis is supported by the progressive decreasing of the seismic activity after the opening of the eruptive fissures (Alparone et al., 2020).

With this challenging work we have, on one hand, reconstructed a fairly precise temporal evolution of the 24–25 December intrusive process. On the other, we have also pointed out that the more the available measurements are heterogeneous and detailed in time and space, the more difficult it is to find the proper model to explain all the data simultaneously. The detailed multiparametric view shows the complexity of the real volcanic processes and the current lack of models able to handle such complexity. In conclusion, in this complex evolutionary framework, the continuous multidisciplinary system has made it possible to (i) provide an early but also reliable model of the source through the interpretation of the displacement pattern (CGPS), and (ii) allow a more detailed and complete model through the integration of all the continuous data (CGPS, borehole strainmeters, and tiltmeters), thereby unraveling each single phenomenon of the entire temporal chain of events.

Data Availability Statement

The geophysical data can be accessed from the platform Figshare (https://doi.org/10.6084/m9.figshare.10292771).

Acknowledgments
We kindly acknowledge F. Guglielmino and A. Bonforte for the fruitful discussions that helped us improve the modeling. We are indebted to the technicians and technologists of the INGV, Osservatorio Etneo for enabling and improving the acquisition of tilt, strain, and GPS data. Finally, we thank Stephen Conway for correcting the English version of our manuscript.

References

Aloisi, M., Bonaccorso, A., Cannavò, F., & Currenti, G. M. (2018). Coupled short- and medium-term geophysical signals at Etna volcano: Using deformation and strain to infer magmatic processes from 2009 to 2017. *Frontiers in Earth Science*, *6*, 109. https://doi.org/10.3389/feart.2018.00109

Aloisi, M., Bonaccorso, A., Cannavò, F., Gambino, S., Mattia, M., Puglisi, G., & Boschi, E. (2009). A new dike intrusion style for the Mount Etna may 2008 eruption modelled through continuous tilt and GPS data. *Terra Nova*, *21*(4), 316–321. https://doi.org/10.1111/j.1365-3121.2009.00889.x

Aloisi, M., Bonaccorso, A., & Gambino, S. (2006). Imaging composite dike propagation (Etna, 2002 case). *Journal of Geophysical Research*, *111*, B06404. https://doi.org/10.1029/2005JB003908

Aloisi, M., Bonaccorso, A., Gambino, S., Mattia, M., & Puglisi, G. (2003). Etna 2002 eruption imaged from continuous tilt and GPS data. *Geophysical Research Letters*, *30*(23), 2214. https://doi.org/10.1029/2003GL018896

Aloisi, M., Jin, S., Pulvirenti, F., & Scaltrito, A. (2017). The December 2015 Mount Etna eruption: An analysis of inflation/deflation phases and faulting processes. *Journal of Geodynamics*, *107*, 34–45. https://doi.org/10.1016/j.jog.2017.03.003

Aloisi, M., Mattia, M., Ferlito, C., Palano, M., Bruno, V., & Cannavò, F. (2011). Imaging the multi-level magma reservoir at Mt. Etna volcano (Italy). *Geophysical Research Letters*, *38*, L16306. https://doi.org/10.1029/2011GL048488

Aloisi, M., Mattia, M., Monaco, C., & Pulvirenti, F. (2011). Magma, faults, and gravitational loading at Mount Etna: The 2002–2003 eruptive period. *Journal of Geophysical Research*, *116*, B05203. https://doi.org/10.1029/2010JB007909

Aloisi, M., Bonaccorso, A., Cannavò, F., Currenti, G., & Gambino, S. (2019). The Dec 24, 2018 eruptive intrusion at Etna volcano revealed and imaged by multi-disciplinary deformation networks (borehole tiltmeters, borehole strainmeters, continuous GPS, mobile GPS, InSAR), Geoph. Res. Abstracts, Vol. 21, EGU2019–7429, 2019 EGU General Assembly 2019.

Alparone, S., Barberi, G., Giampiccolo, E., Maiolino, V., Mostaccio, A., Musumeci, C., et al. (2020). Seismological constraints on the 2018 Mt. Etna (Italy) flank eruption and implications for the flank dynamics of the volcano. *Terra Nova*, *11*, 1271–1282. https://doi.org/10.1111/ter.12463

Bock, Y., de Jonge, P. J., Honcik, D., Bevis, M., Bock, L., & Wilson, S. (2001). Epoch-By-EpochTM Positioning applied to dam deformation monitoring At Diamond Valley Lake, Southern California. *Proceedings of 10th FIG International Symposium on Deformation Measurements (Orange, CA), 78–87*.

Bonaccorso, A. (2001). Mt. Etna volcano: Modelling of ground deformation patterns of recent eruptions and considerations on the associated precursors. *Journal of Volcanology and Geothermal Research*, *109*(1-3), 99–108. https://doi.org/10.1016/S0377-0273(00)00306-1

Bonaccorso, A., Aloisi, M., & Mattia, M. (2002). Dike emplacement forerunning the Etna July 2001 eruption modeled through continuous tilt and GPS data. *Geophysical Research Letters*, *29*(13), 1624. https://doi.org/10.1029/2001GL014397

Bonaccorso, A., & Calvari, S. (2013). Major effusive eruptions and recent lava fountains: Balance between expected and erupted magma volumes at Etna volcano. *Geophysical Research Letters*, *40*, 6069–6073. https://doi.org/10.1002/2013GL058291

Bonaccorso, A., & Calvari, S. (2017). A new approach to investigate an eruptive paroxysmal sequence using camera and strainmeter networks: Lessons from the 3–5 December 2015 activity at Etna volcano. *Earth and Planetary Science Letters*, *475*, 231–241. https://doi.org/10.1016/j.epsl.2017.07.020

Bonaccorso, A., Calvari, S., Currenti, G., Del Negro, C., Ganci, G., Linde, A., et al. (2013). From source to surface: Dynamics of Etna's lava fountains investigated by continuous strain, magnetic, ground and satellite thermal data. *Bulletin of Volcanology*, *75*(2), 690. https://doi.org/10.1007/s00445-013-0690-9

Bonaccorso, A., Calvari, S., Linde, A., & Sacks, S. (2014). Eruptive processes leading to the most explosive lava fountain at Etna volcano: The 23 November 2013 episode. *Geophysical Research Letters*, *41*, 4912–4919. https://doi.org/10.1002/2014GL060623

Bonaccorso, A., Campisi, O., Falzone, G., & Gambino, S. (2004). *Continuous tilt monitoring: a lesson from 20 years experience at Mt. Etna*, *Geophysical Monograph of American Geophysical Union "Etna: Volcano Laboratory"* (Vol. 143, pp. 307–320). Washington, DC: American Geophysical Union. https://doi.org/10.1029/143GM19

Bonaccorso, A., Cannata, A., Corsaro, A., Di Grazia, G., Gambino, S., Greco, F., et al. (2011). Multidisciplinary investigation on a lava fountain preceding a flank eruption: The 10 May 2008 Etna case. *Geochemistry, Geophysics, Geosystems*, *12*, Q07009. https://doi.org/10.1029/2010GC003480

Bonaccorso, A., Currenti, G., Linde, A., & Sacks, S. (2013). New data from borehole strainmeters to infer lava fountain sources (Etna 2011–2012). *Geophysical Research Letters*, *40*, 3579–3584. https://doi.org/10.1002/grl.50692

Bonaccorso, A., Linde, A., Currenti, G., Sacks, S., & Sicali, A. (2016). The borehole dilatometer network of Mount Etna: A powerful tool to detect and infer volcano dynamics. *Journal of Geophysical Research: Solid Earth*, *121*(6), 4655–4669. https://doi.org/10.1002/2016jb012914

Bonforte, A., Bonaccorso, A., Guglielmino, F., Palano, M., & Puglisi, G. (2008). Feeding system and magma storage beneath Mt. Etna as revealed by recent inflation/deflation cycles. *Journal of Geophysical Research*, *113*, B05406. https://doi.org/10.1029/2007JB005334

Bonforte, A., Gambino, S., & Neri, M. (2009). Intrusion of eccentric dikes: The case of the 2001 eruption and its role in the dynamics of Mt. Etna volcano. *Tectonophysics*, *471*(1-2), 78–86. https://doi.org/10.1016/j.tecto.2008.09.028

Bonforte, A., Guglielmino, F., & Puglisi, G. (2019). Large dyke intrusion and small eruption: The December 24, 2018 Mt. Etna eruption imaged by Sentinel-1 data. *Terra Nova*, *31*, 405–412. https://doi.org/10.1111/ter.12403

Branca, S., Coltelli, M., Groppelli, G., & Lentini, F. (2011). Geological map of Etna volcano, 1:50,000 scale. *Italian Journal of Geosciences*, *130*(3), 265–291. https://doi.org/10.3301/IJG.2011.15

Calvari, S., Bilotta, G., Bonaccorso, A., Caltabiano, T., Cappello, A., Corradino, C., et al. (2020). The VEI 2 Christmas 2018 Etna eruption: A small but intense eruptive event or the starting phase of a larger one? *Remote Sensing*, *12*, 905. https://doi.org/10.3390/rs1206905

Calvari, S., Cannavò, F., Bonaccorso, A., Spampinato, L., & Pellegrino, A. G. (2018). Paroxysmal explosions, lava fountains and ash plumes at Etna volcano: Eruptive processes and Hazard implications. *Frontiers in Earth Science*, *6*, 107. https://doi.org/10.3389/feart.2018.00107

Cannavò, F. (2019). A new user-friendly tool for rapid modelling of ground deformation. *Computers & Geosciences*, *128*, 60–69. https://doi.org/10.1016/j.cageo.2019.04.002

Cannavò, F., Camacho, A. G., González, P. J., Mattia, M., Puglisi, G., & Fernández, J. (2015). Real Time Tracking of Magmatic Intrusions by means of Ground Deformation Modeling during Volcanic Crises. *Scientific Reports*, *5*(1), https://doi.org/10.1038/srep10970

Cannavò, F., Sciotto, M., Cannata, A., & Di Grazia, G. (2019). An integrated geophysical approach to track magma intrusion: The 2018 Christmas Eve eruption at Mount Etna. *Geophysical Research Letters*, *46*, 8009–8017. https://doi.org/10.1029/2019GL083120

Carbone, D., Aloisi, M., Vinciguerra, S., & Puglisi, G. (2014). Stress, strain and mass changes at Mt. Etna during the period between the 1991–93 and 2001 flank eruptions. *Earth-Science Reviews*, *138*, 454–468. https://doi.org/10.1016/j.earscirev.2014.07.004

Catalano, S., Bonforte, A., Guglielmino, F., Romagnoli, G., Tarsia, C., & Tortorici, G. (2013). The influence of erosional processes on the visibility of Permanent Scatterers Features from SAR remote sensing on Mount Etna (E Sicily). *Geomorphology*, *198*, 128–137. https://doi.org/10.1016/j.geomorph.2013.05.020

Civico, R., Pucci, S., Nappi, R., Azzaro, R., Villani, F., Pantosti, D., et al. (2019). Surface ruptures following the 26 December 2018, *Mw* 4.9, Mt. Etna earthquake, Sicily (Italy). *Journal of Maps*, *15*(2), 831–837. https://doi.org/10.1080/17445647.2019.1683476

Cocina, O., Neri, G., Privitera, E., & Spampinato, S. (1997). Stress tensor computations in the Mount Etna area (southern Italy) and tectonic implications. *Journal of Geodynamics*, *23*(2), 109–127. https://doi.org/10.1016/S0264-3707(96)00027-0

Cocina, O., Neri, G., Privitera, E., & Spampinato, S. (1998). Seismogenic stress field beneath Mt. Etna (south Italy) and possible relationships with volcano-tectonic features. *Journal of Volcanology and Geothermal Research*, *83*(3-4), 335–348. https://doi.org/10.1016/S0377-0273(98)00026-2

Currenti, G., & Bonaccorso, A. (2019). Cyclic magma recharge pulses detected by high-precision strainmeter data: The case of 2017 inter-eruptive activity at Etna volcano. *Scientific Reports*, *9*, 7533. https://doi.org/10.1038/s441598-01944066-w

Currenti, G., Bonaccorso, A., Del Negro, C., Guglielmino, F., Scandura, D., & Boschi, E. (2010). FEM-based inversion for heterogeneous fault mechanisms: application at Etna volcano by DInSAR data. *Geophysical Journal International*, *183*(2), 765–773. https://doi.org/10.1111/j.1365-246x.2010.04769.x

Currenti, G., Del Negro, C., Ganci, G., & Scandura, D. (2008). 3D numerical deformation model of the intrusive event forerunning the 2001 Etna eruption. *Physics of the Earth and Planetary Interiors*, *168*(1-2), 88–96. https://doi.org/10.1016/j.pepi.2008.05.004

Currenti, G., Napoli, R., Di Stefano, A., Greco, F., & Del Negro, C. (2011). 3D integrated geophysical modeling for the 2008 magma intrusion ad Etna: Constraints on rheology and dike overpressure. *Physics of the Earth and Planetary Interiors*, *185*(1-2), 44–52. https://doi.org/10.1016/j.pepi.2011.01.002

Currenti, G., Solaro, G., Napoli, R., Pepe, A., Bonaccorso, A., Del Negro, C., & Sansosti, E. (2012). Modeling of ALOS and COSMO-SkyMed satellite data at Mt Etna: Implications on relation between seismic activation of the Pernicana fault system and volcanic unrest. *Remote Sensing of Environment*, *125*, 64–72. https://doi.org/10.1016/j.rse.2012.07.008

Currenti, G., Zuccarello, L., Bonaccorso, A., & Sicali, A. (2017). Borehole Volumetric Strainmeter Calibration From a Nearby Seismic Broadband Array at Etna Volcano. *Journal of Geophysical Research: Solid Earth*, *122*(10), 7729–7738. https://doi.org/10.1002/2017jb014663

De Novellis, V., Atzori, S., De Luca, C., Manzo, M., Valerio, E., Bonano, M., et al. (2019). DInSAR analysis and analytical modeling of Mount Etna displacements: The December 2018 volcano-tectonic crisis. *Geophysical Research Letters*, *46*, 5817–5827. https://doi.org/10.1029/2019GL082467

Efron, B. (1982). *The Jacknife, bootstrap and other resampling plans*. Philadelphia: Society for Industrial and Applied Mathematics. https://doi.org/10.1137/1.9781611970319

Ferro, A., Gambino, S., Panepinto, S., Falzone, G., Laudani, G., & Ducarme, B. (2011). High precision tilt observation at Mt. Etna volcano, Italy. *Acta Geophysica*, *59*(3), 618–632. https://doi.org/10.2478/s11600-011-0003-7

Gambino, S., Aloisi, M., Di Grazia, G., Falzone, G., Ferro, A., & Laudani, G. (2019). Ground deformation detected by permanent tiltmeters on Mt. Etna summit: The August 23–26, 2018, Strombolian and effusive activity case. *International Journal of Geophysics*, *2019*, 1–10. https://doi.org/10.1155/2019/1909087

Gambino, S., & Cammarata, L. (2017). Tilt measurements on volcanoes: More than a hundred years of recordings. *Italian Journal of Geosciences*, *136*(2), 275–295. https://doi.org/10.3301/IJG.2017.07

Gambino, S., Falzone, G., Ferro, A., & Laudani, G. (2014). Volcanic processes detected by tiltmeters: A review of experience on Sicilian volcanoes. *Journal of Volcanology and Geothermal Research*, *271*, 43–54. https://doi.org/10.1016/j.jvolgeores.2013.11.007

Giampiccolo, E., Cocina, O., De Gori, P., & Chiarabba, C. (2020). Dyke intrusion and stress-induced collapse of volcano flanks: The example of the 2018 event at Mt. Etna (Sicily, Italy). *Scientific Reports*, *10*, 6373. https://doi.org/10.1038/s41598-020-63371-3

Goldberg, D. E. (1989). *Genetic algorithms in search, optimization and machine learning*. Boston, MA: Kluwer Academic Publishers. ISBN-13: 978-0201157673

Gonzalez, P. J., & Palano, M. (2014). Mt. Etna 2001 eruption: New insights into the magmatic feeding system and the mechanical response of the western flank from a detailed geodetic dataset. *Journal of Volcanology and Geothermal Research*, *274*, 108–121. https://doi.org/10.1016/j.jvolgeores.2014.02.001

Gvirtzman, Z., & Nur, A. (1999). The formation of Mount Etna as the consequence of slab rollback. *Nature*, *401*(6755), 782–785. https://doi.org/10.1038/44555

Hirn, A., Nicolich, R., Gallart, J., Laigle, M., Cernobori, L., & ETNASEIS Scientific Group (1997). Roots of Etna volcano in faults of great earthquakes, Earth Planet. *Science Letters*, *148*, 171–191. https://doi.org/10.1016/S0012-821X(97)00023-X

Jaupart, C., & Vergniolle, S. (1988). Laboratory models of Hawaiian and Strombolian eruptions. *Nature*, *331*(6151), 58–60. https://doi.org/10.1038/331058a0

Laiolo, M., Ripepe, M., Cigolini, C., Coppola, D., Della, S. M., Genco, R., et al. (2019). Space- and ground-based geophysical data tracking of magma migration in shallow feeding system of Mount Etna volcano. *Remote Sensing*, *11*, 1182, Special Issue "Remote Sensing of Volcanic Processes and Risk". https://doi.org/10.3390/rs11101182

Lewis, R. M., & Torczon, V. (1999). Pattern search algorithms for bound constrained minimization. *SIAM Journal on Optimization*, *9*(4), 1082–1099. https://doi.org/10.1137/S1052623496300507

McTigue, D. F. (1987). Elastic stress and deformation near a finite spherical magma body: Resolution of the point source paradox. *Journal of Geophysical Research*, *92*(B12), 12931. https://doi.org/10.1029/jb092ib12p12931

Mogi, K. (1958). Relations between the eruptions of various volcanoes andthe deformations of the ground surface around them. *Bulletin. Earthquake Research Institute, University of Tokyo*, *36*, 99–134.

Nikolaidis, R. M., Bock, Y., de Jonge, P. J., Shearer, P., Agnew, D. C., & Van Domselaar, M. (2001). Seismic wave observations with the Global Positioning System. *Journal of Geophysical Research: Solid Earth*, *106*(B10), 21,897–21,916. https://doi.org/10.1029/2001jb000329

Okada, Y. (1985). Surface deformation due to shear and tensile fault in half-space. *Bulletin of the Seismological Society of America*, *75*, 1135–1154.

Palano, M., Viccaro, M., Zuccarello, F., & Gresta, S. (2017). Magma transport and storage at Mt. Etna (Italy): A review of geodetic and petrological data for the 2002–03, 2004 and 2006 eruption. *Journal of Volcanology and Geothermal Research*, *347*, 149–164. https://doi.org/10.1016/j.jvolgeores.2017.09.009

Tiampo, K. F., Rundle, J. B., Fernandez, J., & Langbein, J. O. (2000). Spherical and ellipsoidal volcanic sources at Long Valley caldera, California, using a genetic algorithm inversion technique. *Journal of Volcanology and Geothermal Research*, *102*(3-4), 189–206. https://doi.org/10.1016/S0377-0273(00)00185-2